Numerical Simulation of Sliding Drops on an Inclined Solid Surface

Marco Maglio and Dominique Legendre

Abstract We consider numerical simulations of drops sliding on an inclined solid surface. The simulations are performed using our in house research code JADIM based on the Volume of Fluid formulation of the mass and momentum equations. Special algorithms have been developed for the simulation of the hysteresis of the contact line as well as for the description of moving contact lines. The onset of motion is analyzed and the effect of the contact line hysteresis is studied. The critical angle of inclination, as well as the corresponding drop shape, are discussed and compared with previous experiments. The sliding velocity for a constant angle of inclination is also considered and compared with experiments. The different shapes observed in experiments (rounded, corner, cusp, or pearling drop) are recovered depending on both the fluid properties and the angle of inclination. The drop sliding velocity is then considered for larger values of the hysteresis.

1 Introduction

Motion of drops on surfaces is a phenomenon observed in everyday life as well as in many environmental or industrial applications: coating processes, combustion processes, pesticide and insecticide pulverization on cultivations, lab-on-a-chip devices, etc. In particular, small droplets have the capability to stick on non-horizontal surfaces. Despite its apparent simplicity, the behaviour of a drop on an inclined solid surface is far to be completely understood. It involves static, hysteresis, and dynamic contact line behaviours. Depending on the fluid properties, the hysteresis and the wall

M. Maglio · D. Legendre (✉)
Institut de Mécanique des Fluides de Toulouse, IMFT, Université de Toulouse, CNRS-INPT-UPS, 2 Allée du Professeur Camille Soula, Toulouse 31400 , France
e-mail: marco.maglio@imft.fr

D. Legendre
e-mail: dominique.legendre@imft.fr

L. Di G. Sigalotti et al. (eds.), *Computational and Experimental Fluid Mechanics with Applications to Physics, Engineering and the Environment*, Environmental Science and Engineering,
DOI:10.1007/978-3-319-00191-3_3,

inclination, different drop shapes (rounded, corner, or pearling drop) can be observed (Le Grand et al. 2005). In addition, its numerical modelling is still a great challenge. For example, up to now the different sliding regimes observed in the experiments have not been reproduced by numerical simulations.

From the numerical point of view, the description of a moving contact line cannot be performed by direct discretization of the equations. Indeed, the solution of the Navier-Stokes equations gives an infinite viscous dissipation at the moving contact line when a no-slip condition is applied on the wall (Huh and Scriven 1971). As a consequence, refining a grid induces a divergence of the viscous stress at the contact line (Afkhami et al. 2009).

In order to be predictive (i.e., with no adjustable parameters), numerical simulations of moving contact lines at the macroscopic scale must describe correctly the contact angle and the contact line speed. A full numerical simulation would consist in resolving all scales involved in the problem, i.e., from the macro scale L to the nano-metric scale associated with the effective slip length λ. For example, let us consider a millimeter-size droplet as studied in this work with an equivalent radius $a = (3V/4\pi)^{1/3} \approx 1$ mm, where V is the drop volume. The full resolution of all scales involved in this problem would require $N_{2D} \approx (R/\lambda)^2 \approx 10^{12}$ nodes for a 2D simulation and $N_{3D} \approx (R/\lambda)^3 \approx 10^{18}$ nodes for a 3D simulation. Such a grid size is obviously not compatible with the present computer's resources and/or requires an extremely long CPU time even on parallel computers. Consequently, it is clear that the simulation of the contact line hydrodynamics can not be performed up to the nano-scale level for a millimeter size drop. For $L = \mathrm{O}(1)$ mm, the grid size Δ is limited to some microns. In contrast, Molecular Dynamics simulations are able to describe the nano-scale effects (Blake 2006), but due to the limited computer resources, the size of the macro scale is limited and simulations are only possible for nano-drops (Winkels et al. 2012).

Different approaches can be used to overcome the singularity at the contact line (Bonn et al. 2009). The hydrodynamic models are based on analytical solutions of the interface shape, while the contact line velocity U_{cl} is obtained by matching methods. Typically, an inner region, whose characteristic length is imposed by the slip length λ, is matched to an outer region (the apparent region) of characteristic size L where no-slip occurs. Assuming Stokes flow at both scales, the apparent or dynamic contact angle θ_d is found to be a function of the wall contact angle θ_W (considered to be constant), the capillary number $\mathrm{Ca} = \mu_d U_{cl}/\sigma$, the logarithm of the scale ratio $\ln(L/\lambda)$, and the viscosity ratio q (Voinov 1976; Dussan 1976; Cox 1986). We have developed a sub-grid model of moving contact lines based on this matching relation between the molecular wetting at the nano-scale (not solved) and the macro-scale that is solved.

The paper is decomposed as follows. The problem considered in this paper is presented in Sect. 2. The numerical code JADIM as well as the numerical modelling developed for the static, hysteresis, and dynamic contact angle, are described in Sect. 3. Section 4 reports experimental tests concerning the onset of motion of a drop deposited on a inclined wall. Section 5 presents the simulation concerning the sliding regime and Sect. 6 contains the conclusions.

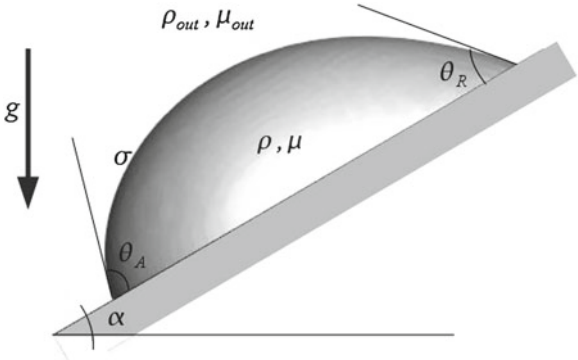

Fig. 1 Definition of parameters for a drop on an inclined surface

2 Statement of the Problem

We consider a drop of volume $V = 4\pi a^3/3$ (where a is the equivalent radius used as the characteristic length scale) located on a inclined surface (see Fig. 1). We denote by ρ_L, μ_L, and σ the drop density, the drop viscosity, and the surface tension of the interface between the drop and the air, respectively. Here ρ_G and μ_G denote the density and viscosity of the air. The surface wettability is characterized by the advancing θ_A and receding θ_R contact angles. The inclination is characterized by the angle α made by the surface and the horizontal. With the density and viscosity ratios, ρ_G/ρ_L and μ_G/μ_L, being much smaller than unity, the problem is completely characterized by the introduction of two additional dimensionless numbers, namely the Eötvös number $\mathrm{Eo} = \rho g a^2/\sigma$ and the Morton number $\mathrm{Mo} = \mu_L^4 g/\rho_L \sigma^3$. The values of the Ohnesorge number $\mathrm{Oh} = \mu_L/\sqrt{\rho_L \sigma a}$ are also specified.

Two series of numerical experiments are presented. In Sect. 4, we first focus on the angle and the drop shape at the onset of motion. At time $t = 0$, the drop is a hemispherical cap (the initial contact angle is $\theta_i = 90°$) and the wall is horizontal ($\alpha = 0$). Once the drop shape is stabilized, the wall is inclined at $t = t_0$, following a linear time evolution given by $\alpha(t) = \pi(t - t_0)/T$. The characteristic time T of the inclination is chosen to be much larger than the physical times of the problem, i.e. the visco-capillary time $t_\mu \approx \mu_L a/\sigma$ and the inertia-capillary time $t_i \approx \sqrt{\rho_L a^3/\sigma}$. In practice, T is chosen such that $T > 10 \max(t_\mu, t_i)$. The angle at the onset of motion is denoted by α_c and corresponds to the angle when the advancing and receding points of the drop are both moving in the direction of sliding.

In Sect. 5, we consider the sliding velocity of a drop on a surface with a fixed angle of inclination α. The drop is initially a hemispherical cap making a contact angle $\theta_i = 50°$ with the wall. We record the time evolution of the drop velocity and determine the sliding velocity corresponding to the steady state once gravity balances capillary and viscous forces.

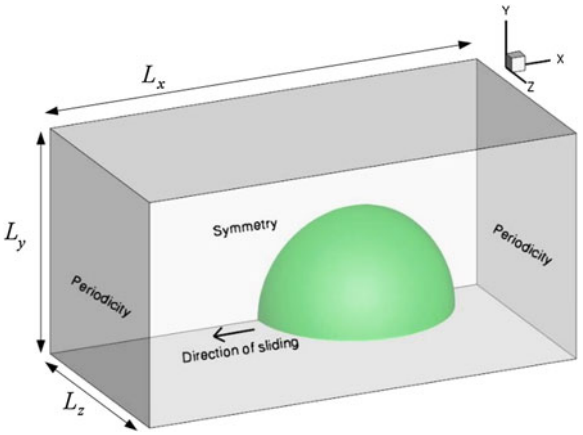

Fig. 2 Domain definition and initial layout of the simulations

For each simulation, a cap of initial radius $R_0 = a\left[2/(2-3\cos\theta_i+\cos^3\theta_i)\right]^{1/3}$ is deposited on the surface. We define x as the direction of sliding along the plane, y as the normal direction of the plane, and z as the lateral direction. Since the plane (x, y) is a symmetry plane for the problem, the computational domain shown in Fig. 2 is reduced to half the space as defined by $z \geq 0$. The dimensions of the computational domain are $L_x = 6.5\,a$ and $L_y = L_z = 2.25\,a$, where L_x, L_y, and L_z are the domain sizes along the x-, y-, and z-directions, respectively. A symmetry condition is thus imposed on the plane (x, y) and periodicity is enforced on both sides of the box in the sliding direction, allowing for long-term simulations in a reduced domain. For pearling drops, as described in Sect. 5, the length L_x of the domain was doubled, i.e. $L_x = 13\,a$.

3 Numerical Code

3.1 Volume of Fluid (VoF) Solver

The numerical simulations reported in this work were performed using the Volume of Fluid (VoF) solver developed in the JADIM code (Bonometti and Magnaudet 2007; Dupont and Legendre 2010). The one-fluid exact system of equations is obtained by introducing the distribution C, which is used to localize one of the two phases. In this study, we define C as $C = 1$ within the liquid drop, and $C = 0$ for the external fluid. The one-fluid function C makes possible the definition of the one-fluid variables $U = CU_L + (1-C)U_G$ for the velocity, $P = CP_L + (1-C)P_G$ for the pressure, $\rho = C\rho_L + (1-C)\rho_G$ for the density, and $\mu = C\mu_L + (1-C)\mu_G$ for the viscosity. The position of the interface is then given by the transport equation:

$$\frac{\partial C}{\partial t} + U \cdot \nabla C = 0. \tag{1}$$

The two fluids are assumed to be Newtonian and incompressible, with no phase change. Under isothermal conditions and in the absence of any surfactant, the surface tension is constant and uniform at the interface between the two fluids. Under these conditions, the velocity field U and the pressure P satisfy the classical one-fluid formulation of the Navier-Stokes equations:

$$\nabla \cdot U = 0, \tag{2}$$

$$\rho \left(\frac{\partial U}{\partial t} + U \cdot \nabla U \right) = -\nabla P + \nabla \cdot \Sigma + \rho g + F_\sigma, \tag{3}$$

where Σ is the viscous stress tensor, g is the gravity, and F_σ is the capillary force contribution given by

$$F_\sigma = \sigma \, (\nabla \cdot n) \, n \delta_I, \tag{4}$$

where σ is the surface tension, n denotes the outward unit vector normal to the drop surface, and δ_I is the Dirac distribution associated to the interface position.

The system of Eqs. (1)–(3) is discretized using the finite volume method and time is advanced through a third-order Runge-Kutta scheme for the viscous stresses. Incompressibility is satisfied at the end of each time step through a projection method. The overall algorithm is second-order accurate in both time and space. The volume fraction C and the pressure P are volume-centred, while the velocity components are face-centred. Due to the discretization of C, the interface is numerically represented by a surface of finite thickness and cells cut by the interface correspond to regions with $0 < C < 1$. One important aspect of our approach compared to the classical VoF or Level Set methods (Sussman et al. 1998; Scardovelli and Zaleski 1999; Sethian 1999) concerns the technique used to control the stiffness of the interface. In our approach no interface reconstruction or redistancing techniques are employed. The interface location and stiffness are both controlled by an accurate transport algorithm based on an FCT (Flux-Corrected-Transport) scheme (Zalesak 1979). This method leads to an interface thickness of about three grid cells by the implementation of a specific procedure to calculate the velocity used to transport C in flow regions of strong strain and shear (Bonometti and Magnaudet 2007).

The numerical description of the surface tension is one crucial point when we consider systems where capillary effects control the interface shape. This interfacial force is solved using the classical CSF (Continuum Surface Force) model (Brackbill et al. 1992):

$$F_\sigma = \sigma \nabla \cdot \left(\frac{\nabla C}{\| \nabla C \|} \right) \nabla C. \tag{5}$$

A classical problem connected to this formulation is the generation of spurious currents (Lafaurie et al. 1994; Popinet and Zaleski 1999). In order to decrease the inten-

sity of spurious currents, a classical solution, introduced by Brackbill et al. (1992), is employed which consists in calculating the surface curvature from a smoothed density gradient, while the discretization of the delta function uses an non-smoothed density. The spurious currents have been characterized by Dupont and Legendre (2010). Their maximum magnitude is shown to evolve as $0.004\sigma/\mu$, in agreement with other codes that use the Brackbill's formulation.

3.2 Numerical Modelling of the Contact Angle

The aim of the numerical method is to handle static (either with or without hysteresis) and dynamic contact lines. The method has been developed to simulate the transition from a static contact line in the hysteresis range to a moving contact line and vice versa. The numerical scheme used in this study has been initiated by Dupont and Legendre (2010) for 2D and axisymmetric geometries. It has also been used to study droplet spreading in axisymmetry (Legendre and Maglio 2013). In this paper, the method is extended to 3D geometries.

The calculation of the capillary term requires the knowledge of the contact angle made by the interface at the wall. Indeed, the capillary contribution (5) in the momentum equation requires the knowledge of ∇C. Since $\nabla C/\|\nabla C\|$ is the unit vector normal to the interface, the boundary condition for ∇C is thus given directly by the value of the contact angle θ_W, as shown by the following relation:

$$\frac{\nabla C}{\|\nabla C\|} = \mathbf{n} = \sin\theta_W \mathbf{n}_{\|} + \cos\theta_W \mathbf{n}_{\perp}, \tag{6}$$

where $\mathbf{n}_{\|}$ and $\mathbf{n}_{\perp}$ are the unit vector components of the normal vector parallel and perpendicular to the wall.

The general method is divided into two steps. We first determine the value of the contact angle to be applied at the wall. This value is then imposed as a boundary condition using relation (6) for the calculation of the capillary contribution (5) in the momentum balance equation (3).

Static contact angle

The static equilibrium of a drop on an horizontal wall is characterized by the static contact angle θ_S between the interface and the wall. A simple force balance at the interface gives the Young-Dupré relation:

$$\sigma\cos\theta_S = -\sigma_{SG} - \sigma_{SL}, \tag{7}$$

where σ_{SL}, σ_{SG}, and σ are, respectively, the values of surface tension for the solid/liquid, solid/gas, and gas/liquid interfaces. The value of the static contact angle θ_S is a parameter of the simulation, characterizing the fluid-fluid-wall wettability. Simulations can also be performed by imposing a constant contact angle. This is the simplest situation in which relation (6) is used by imposing $\theta_W = \theta_S$. In Dupont

and Legendre (2010), some simulations have been performed by imposing a static contact angle θ_S in order to compare with the dynamic models.

Dynamic contact line

As was outlined in the introduction, direct numerical simulations that resolve all scales involved in the problem are not possible. In particular, simulations of contact line hydrodynamics cannot be performed up to the nano-scale. A sub-grid description, as introduced by Dupont and Legendre (2010), must be implemented for macroscopic simulations of problems controlled by moving contact lines. This description, which is implemented in JADIM, aims to correctly reproduce the physics at the contact line. The model is based on considerations at the macroscopic scale based on the analytical derivation by Cox (1986) that connect the macroscopic region (imposed by the grid resolution Δ) to the inner region (imposed by the slip length λ). Thus, at the macroscopic scale, the wall condition seen by the fluid is a no-slip boundary condition:

$$U_W = 0. \tag{8}$$

This consists in imposing a zero numerical slip length $\lambda_N = 0$. At the macroscopic level, the interface shape characterized by the dynamic apparent contact angle θ_d is connected to the microscopic contact angle θ_S by means of the relation (Cox 1986):

$$g(\theta_d) - g(\theta_S) = \mathrm{Ca}\ln(\frac{L}{\lambda}), \tag{9}$$

for two fluids of arbitrary viscosity, where $g(\theta)$ is a function that simplifies to:

$$g(\theta) = \int_0^\theta \frac{x - \sin x \cos x}{2\sin x} dx, \tag{10}$$

when the surrounding fluid is of much smaller viscosity (for example, the air). In practice, the functions $g(x)$ and $g(x)^{-1}$ can be approximated with good accuracy by means of a fitting polynomial (Dupont and Legendre 2010). When the condition $\theta_d < 3\pi/4$ is satisfied, Eq. (9) reduces to the well-known Cox-Voinov relation: $\theta_d^3 = \theta_S^3 + \mathrm{Ca}\ln(L/\lambda)$ (Voinov 1976; Cox 1986). In relation (9), L is imposed by the grid spacing and λ is the physical slip length. Due to the use of a staggered grid, where the VoF function C is located at the centre of the volume, while the velocities are face-centred, the interface is transported by the velocity a distance $\Delta/2$ and therefore one has $L = \Delta/2$. Several experiments have demonstrated that the apparent region is characterized by $L \approx 10\,\mu\mathrm{m}$ and that the characteristic slip length is $\lambda \approx 1{-}10\,\mathrm{nm}$ (Marsh et al. 1983; Ngan and Dussan 1989; Dussan et al. 1991; Shen and Ruth 1998). More recently, Rio (2005) and Le Grand et al. (2005) have shown that Eq. (9), in its simplified form $\theta_d^3 = \theta_S^3 + 9\mathrm{Ca}\ln(L/\lambda)$, provides a good description of their experiments. The length L is taken as the distance at which the measurement is taken and λ is used as an adjustable parameter. Thus, Rio (2005) showed that for two different measurement techniques the macroscopic length was $L \approx 30\,\mu\mathrm{m}$, using the Laser measurement, and $L \approx 200\,\mu\mathrm{m}$, using the optic circle

technique. From these results, the microscopic length λ was found to be between $\lambda = 7\,\text{nm}$ and $\lambda = 15\,\text{nm}$, depending on the characteristics of the measurement and the model employed to fit the data. The slip length should be intended as the molecular slip, which is of the order of some molecules. Considering the value usually found for water-like liquids on solid substrates (Lauga et al. 2007), we have chosen $\lambda = 10^{-9}$ m in Eq. (9) for the simulations reported in this work.

Several authors have dealt with the "stress singularity" paradox by introducing the Navier slip condition, that gives a relation between the fluid velocity at the wall U_W and a numerical slip length λ_N:

$$U_W = \lambda_N \left(\frac{\partial U}{\partial y} \right)_W . \tag{11}$$

For example, this has been implemented by Renardy et al. (2001) in the case of a VoF scheme and by Spelt (2005) in a Level-Set code. Both of these methods impose a static contact angle θ_S at the wall, assuming that the microscopic contact angle is $\theta_W = \theta_S$. The dynamic contact angle is then obtained solving the full hydrodynamic problem up to a microscopic neighborhood. Unfortunately, due to the grid refinement limitation, these simulations use unrealistically large slip length values and, therefore, the slip length λ_N becomes in practice an adjustable parameter for the simulation (see Bonn et al. (2009) for a similar comment). The grid convergence of the simulations is then reached but an unphysical slip condition is required for this.

Hysteresis of contact angle

A number of numerical calculations has considered the modelling of the dynamic contact angle, while only few studies have implemented models for the hysteresis of the contact line of sessile drops. Some examples can be found in the literature (Dimitrakopoulos and Higdon 1999; Spelt 2005; Fang et al. 2008; Yokoi et al. 2009). All these methods consist in implementing the following conditions for the normal velocity U_{cl} of the contact line:

$$U_{cl} < 0 \quad \text{if} \quad \theta_d < \theta_R, \tag{12}$$

$$U_{cl} = 0 \quad \text{if} \quad \theta_R \leq \theta_d \leq \theta_A, \tag{13}$$

$$U_{cl} > 0 \quad \text{if} \quad \theta_A < \theta_d. \tag{14}$$

The method implemented here makes possible the transition from a static (resp. moving) to a moving (resp. static) contact line. The procedure is divided into two steps:

Step 1: For every cell containing the interface ($0 \leq C \leq 1$), the angle θ^* that cancels the local momentum balance Eq. (3) is determined by an iterative procedure using a simple Newton-Raphson scheme. The iteration is stopped when $\theta^{n+1} - \theta^n < \epsilon_\theta$ with a convergence limit of $\epsilon_\theta = 10^{-4}$.

Step 2. The value of θ^* is compared to the hysteresis range and two possible situations can be found:

(i) the contact angle is inside the hysteresis: $\theta_R \leq \theta^* \leq \theta_A$. The contact line is static and the contact angle is imposed as θ^* so that the momentum balance locally cancels. Thus, if the interface was immobile at the beginning of the time step, it remains immobile for the next time step; if the interface was previously in motion, the interface is stopped.

(ii) the contact angle is outside the hysteresis: $\theta^* < \theta_R$ or $\theta^* > \theta_A$. As a consequence, the contact line cannot be static. The value of the contact angle is then calculated using the dynamic model described above. The static contact angle is the advancing (resp. receding) angle when $\theta^* > \theta_A$ (resp. $\theta^* < \theta_R$).

3.3 Numerical Validation and Grid Convergence

The validation as well as the time and grid convergence of the numerical method used for the simulation of the dynamic contact angle have been extensively discussed in Dupont and Legendre (2010), Maglio (2012), and Legendre and Maglio (2013). Static, hysteresis, and dynamic situations have been considered for spreading drops, drops on inclined surfaces, and drops in a surrounding shear flow. In particular, a very satisfactory agreement has been found with experiments of spreading drops for both water drops and viscous drops. The inertia-capillary regime of spreading characterized by a contact line expansion varying as $t^{1/2}$ and the Tanner's evolution going as $t^{1/10}$ have been recovered. Comparisons of our model with other variants, i.e. static contact angle versus dynamic contact angle and no-slip condition versus slip condition, were also reported by Maglio (2012). These comparisons clearly stress the importance of considering a dynamic model for the simulation of moving contact lines. For the study reported in this paper, additional tests have been performed to ensure grid and time convergence for the onset of motion, as well as for the sliding drop velocity. They are discussed in the sections below.

4 The Onset of Motion

The angle of inclination α_c of the surface at the onset of motion can be obtained by considering the force balance acting on the drop. The volume V of the largest drop that can stick on the surface is given by the balance between the weight of the drop and the interfacial force acting along the contact line cl:

$$\rho g_L V \sin \alpha_c + \sigma \int_{cl} \cos\theta \sin\beta dl = 0, \tag{15}$$

where θ is the local contact angle and β is the angle between the unit normal pointing outwards the drop and the direction perpendicular to the sliding direction. By definition $\beta = 90°$ at the front of the drop and $\beta = -90°$ at the rear. Thus, the above

relation reduces to

$$\rho_L V g \sin\alpha_c = \kappa_c \sigma (\cos\theta_R - \cos\theta_A), \tag{16}$$

where κ_c is the characteristic length κ at the onset of motion, where κ is given by

$$\kappa = -\frac{1}{\cos\theta_R - \cos\theta_A} \int_{cl} \cos\theta \sin\beta dl. \tag{17}$$

Furmidge (1962) found that relation (16) is in excellent agreement with the experiments, if κ is assumed to be the drop width w. As shown by relation (17), κ is not necessarily the drop width because it depends on the contact line shape. Nevertheless, for some particular drop shapes it is possible to demonstrate that $\kappa = w$. This is the case of a spherical cap drop with a small hysteresis range ($\theta_A \approx \theta_R$) and of a parallel sided drop with circular advancing and receding contact lines.

Using the equivalent radius a as the characteristic length, we can rewrite relation (16) in terms of the Eötvös number $\mathrm{Eo} = \rho g a^2/\sigma$:

$$\sin\alpha_c = \frac{\kappa}{a}\frac{3}{4\pi}(\cos\theta_R - \cos\theta_A)\,\mathrm{Eo}^{-1} \tag{18}$$

so that the critical contact angle varies as $(\cos\theta_R - \cos\theta_A)\,\mathrm{Eo}^{-1}$ and depends on the contact line shape.

Much work, mostly experimental, has focused on the characterization of the onset of motion (Bikerman 1950; Rotemberg et al. 1984; Dussan 1985; Milinazzo and Shinbrot 1988; Extrand 1995; Dimitrakopoulos and Higdon 1999; Podgorski 2000; Le Grand et al. 2005). Considering a spherical cap drop with a small value of the contact angle hysteresis (i.e. $\theta_A \approx \theta_R$), Dussan (1985) showed that the onset of motion is described by

$$\sin\alpha_c = \frac{3}{\pi\, 2^{1/3}} \frac{(1+\cos\theta_A)^{1/2}}{(2+\cos\theta_A)^{1/3}\,(1-\cos\theta_A)^{1/6}} (\cos\theta_R - \cos\theta_A)\,\mathrm{Eo}^{-1}. \tag{19}$$

This analytical solution is thus only valid for small values of the hysteresis, with $\theta_A - \theta_R$ being typically less than 10°. Relation (19) indicates that the characteristic length is $\kappa_c = 2^{5/3}(1+\cos\theta_A)^{1/2}\,(2+\cos\theta_A)^{-1/3}\,(1-\cos\theta_A)^{-1/6}\,a$. A plot of this relation as a function of θ_A reveals that the variation is moderate for $30° \le \theta_A \le 145°$ so that in a first approximation κ_c can be expressed using $\theta_A = 90°$:

$$\kappa_c \approx 2^{4/3}\, a. \tag{20}$$

Among the existing experimental studies, here we consider those by Podgorski (2000) and Le Grand et al. (2005), who reported well documented experiments of silicon oil drops deposed on different inclined surfaces. The corresponding experimental conditions are displayed in Fig. 3. We see that these experiments have focused on small hysteresis ranges. The purpose of our study is to compare our simulations

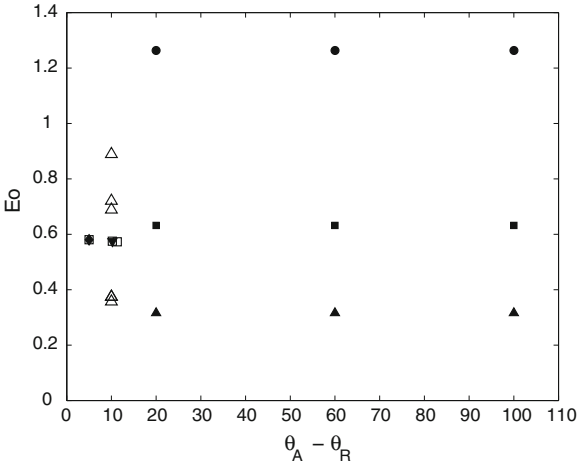

Fig. 3 Phase diagram ($\theta_A - \theta_R$)–Eo for the cases considered. Experiments: □ Le Grand et al. (2005), △ Podgorski (2000). Numerical simulations: ▲ Eo = 0.32 (FL1), ■ Eo = 0.63 (FL2), ● Eo = 1.26 (FL3), ▼ Eo = 0.57 (47V100), ▼ Eo = 0.57 (47V100), and ♦ Eo = 0.58 (47V10)

with the experimental results for this small range of the contact angle hysteresis and then to extend the study to a larger hysteresis range. For the sake of direct comparison, we have considered two situations reported by Le Grand et al. (2005), corresponding to fluids 47V10 and 47V100, with Eötvös numbers of 0.58 and 0.57, and hysteresis ranges of (42.7°, 52.9°) and (45.5°, 50.5°), respectively. We have further extended the experimental studies by considering three larger contact angle hysteresis, i.e., $(\theta_A, \theta_R) = (80°, 100°)$, $(60°, 120°)$, and $(40°, 140°)$, for Eo = 0.32, 0.63, and 1.26. The drop properties used in these simulations are listed in Table 1.

The grid and time convergence is here discussed for fluid FL1 in Table 1. Two regular grids M1 and M2 are considered. They are, respectively, made of $150 \times 50 \times 50$ and $300 \times 100 \times 100$ nodes in the x-, y-, and z-directions. The drop radius a corresponds to 22.5 and 45 nodes, respectively. The grid M1 is first used for discussing the effect of the time step. The simulations produced $\alpha_c = 31.5°$, $\alpha_c = 34.0°$, and $\alpha_c = 34.7°$ for time steps $\Delta t = 2 \times 10^{-5}$ s, 10^{-5} s, and 5×10^{-6} s, respectively.

Table 1 Onset of motion: parameters used for the simulations

Fluid	a (mm)	ρ kg/m^3	μ Pa.s	σ N/m	Eo (-)	Oh (-)	Mo (-)
FL1	0.595	655	0.01	7.2	0.32	0.19	4.0×10^{-4}
FL2	0.595	655	0.0168	3.6	0.63	0.45	3.2×10^{-2}
FL3	0.595	655	0.01	1.8	1.26	0.38	2.6×10^{-2}
47V100	1.127	964	0.103	20.9	0.57	0.68	1.3×10^{-1}
47V10	1.127	936	0.01	20.1	0.58	0.69	1.3×10^{-5}

A simulation performed using grid M2 and $\Delta t = 5 \times 10^{-6}$ s yielded $\alpha_c = 36.0°$, which differs only by ∼3 % from the corresponding value obtained using the grid M1. Therefore, in order to minimize the computational time, the results reported in this section were obtained using $\Delta t = 1 \times 10^{-5}$ s and the mesh M1 ($150 \times 50 \times 50$).

4.1 Drop Shape During Surface Inclination

We first consider the case when Eo = 0.63 and (θ_A, θ_R)=(100°, 80°) (see Table 1) in order to describe the evolution of the shape and the contact angle during the inclination of the surface. Figure 4 shows the shape of the drop from the beginning of the simulation until the onset of motion for different inclinations of the surface. During the tilting of the surface, the drop re-arranges its shape while remaining pinned to the inclined surface. Figure 4h corresponds to the onset of motion and Fig. 4i shows when the drop is sliding.

Figure 5 represents the corresponding evolution of the contact angle at the front and rear points of the drop. As explained in Sect. 2, the surface was inclined after the drop stabilization. This corresponds to the vertical line at $\alpha = 0°$. Then, we can notice that the advancing angle at the front of the drop reaches first the limit value of hysteresis ($\theta_A = 100°$). The onset of motion is observed once the rear contact angle reaches the inferior limit given by the receding angle, here $\theta_R = 80°$. For this case, the sliding happens at 18°. This is confirmed by Fig. 6 (top), where the velocities for the front, rear, and centre of mass of the drop are displayed. We can see that the front contact line and the centre of mass start to move first. The rear stagnation point starts moving at a larger angle, which corresponds to the onset of motion. Figure 6 (bottom) shows the evolution of the contact angle along the contact line as a function of the local angle β between the normal of the contact line and the z-direction, for different inclinations of the surface. Due to the initial condition (the drop is initialized as a spherical cap), the contact angle is everywhere 90°. Then, the contact angle evolves progressively until it reaches the distribution corresponding to the beginning of the sliding, where the advancing and receding limits are clearly observed at the front and the rear of the drop, respectively.

4.2 Angle of Inclination at the Onset of Motion

The shapes of the drops at the onset of motion for all the cases considered are shown in Fig. 7. For each case, the shape is compared with the spherical one at the beginning of the simulation in order to outline the deformation. The value of the critical angle α_c is also shown in the figure. For the smallest Eötvös number Eo = 0.31, with the hysteresis of $\theta_A - \theta_R = 120° - 60°$ and $\theta_A - \theta_R = 140° - 40°$, the drop is found to remain pinned to the wall for the vertical inclination. When the Eötvös number increases, the critical angle α_c decreases, because the drop is more deformed by

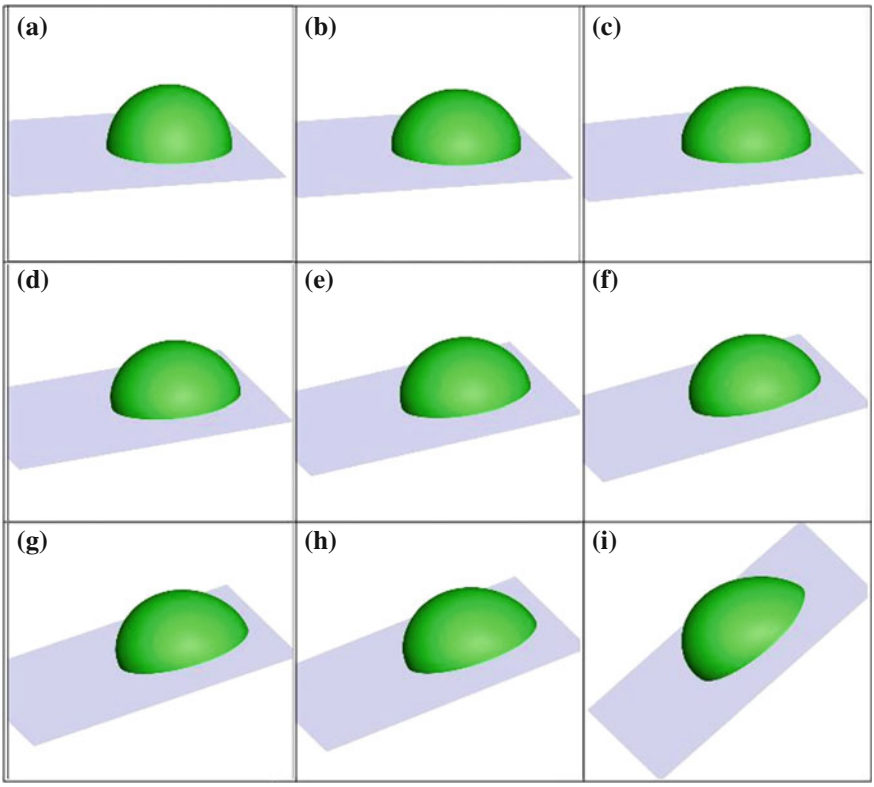

Fig. 4 Eo $= 0.63$ and $\theta_A - \theta_R = 100° - 80°$. Shapes of the drop during the tilting of the surface. **a** beginning of the simulation; **b** $\alpha = 0°$ (end of stabilization); **c** $\alpha = 2°$; **d** $\alpha = 6°$; **e** $\alpha = 9°$; **f** $\alpha = 12°$; **g** $\alpha = 15°$; **h** $\alpha = 18°$ (onset of motion); and **i** $\alpha = 39°$

gravity and reaches faster the shape of motion. As expected, we observe also that the hysteresis range increases the retention force of the drop on the surface.

The angle of inclination α_c at the onset of motion is shown in Fig. 8. Considering the equilibrium force balance (18), the figure shows $\sin \alpha_c$ as a function of $(\cos \theta_R - \cos \theta_A)\mathrm{Eo}^{-1}$. The experimental values of Le Grand et al. (2005) and Podgorski (2000) are also shown for comparison. Surprisingly, all the results seem to collapse on the same evolution whatever are the value of the contact angle hysteresis and the Eötvös numbers considered. For $(\cos \theta_R - \cos \theta_A)\mathrm{Eo}^{-1} \leq 1$, the critical angle is correctly described by relation (18), where the characteristic length $\kappa_c = 2^{4/3}\, a$ is deduced from the analytical relation (19) obtained by Dussan (1985). For larger values of $(\cos \theta_R - \cos \theta_A)\mathrm{Eo}^{-1}$, the numerical results are always under the line representing relation (18) with $\kappa_c = 2^{4/3}\, a$. They correspond to lower values of κ_c, which can be explained by a more elongated shape of the drops. According to Fig. 8, a drop cannot slide on a wall regardless of its inclination if $(\cos \theta_R - \cos \theta_A)\mathrm{Eo}^{-1} \gtrsim 2$.

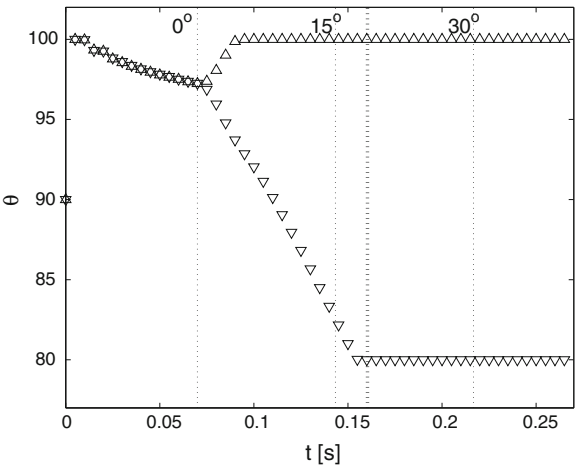

Fig. 5 Eo = 0.63 and $\theta_A - \theta_R = 100° - 80°$. Evolution of the advancing (△) and receding (▽) angles. The corresponding inclination of the surface is shown on the *top* of the graph. The angle at the onset of motion $\alpha_c = 18°$ is shown using a *larger dash line*

5 Sliding Velocity

In this section, we consider the terminal velocity U_T of a drop sliding on a wall with a fixed inclination α. We first compare our simulations with the experiments of Le Grand et al. (2005). Then, we discuss the effect of the contact angle hysteresis on the sliding velocity. The parameters used for the simulations correspond to fluids 47V100 and 47V10, while the drop size is taken from the experiments of Le Grand et al. (2005), (see Table 1). The corresponding contact angle hysteresis ranges (θ_A, θ_R) are (52.9°, 42.7°) and (50.5°, 45.5°), respectively. A spherical cap of volume $V = 6$ mm^3 with a contact angle $\theta_S = 50°$ is assumed as an initial condition (at $t = 0$). The numerical layout of the simulation is identical to the one presented in the previous section. The wall inclination α is fixed during the entire simulation. We have performed simulations for α in the range from α_c to 90°, where α_c is the angle at the onset of motion. We have checked for some cases (typically for the two fluids at $\alpha = 50°$) that the terminal velocity is similar when increasing progressively the wall inclination from 0° to α following the procedure described in the previous section.

In the simulations described here we have used $\Delta t = 1 \times 10^{-5}$ s and mesh M1 ($150 \times 50 \times 50$). The time and grid convergence has also been checked by varying the grid spacing and the time step on the drop velocity. For example, with mesh M1 the terminal velocity of a 47V100 drop is $U_T = 0.00204$ m s^{-1}, $U_T = 0.00188$ m s^{-1}, and $U_T = 0.00179$ m s^{-1} for $\Delta t = 1 \times 10^{-5}$ s, $\Delta t = 0.5 \times 10^{-5}$ s, and $\Delta t = 0.2 \times 10^{-5}$ s, respectively. For a finer grid, say M3, with $225 \times 75 \times 75$ nodes and $\Delta t = 0.2 \times 10^{-5}$ s, the simulation gives $U_T = 0.00199$ m s^{-1}, which implies about a 1 % difference with the value obtained using grid M1.

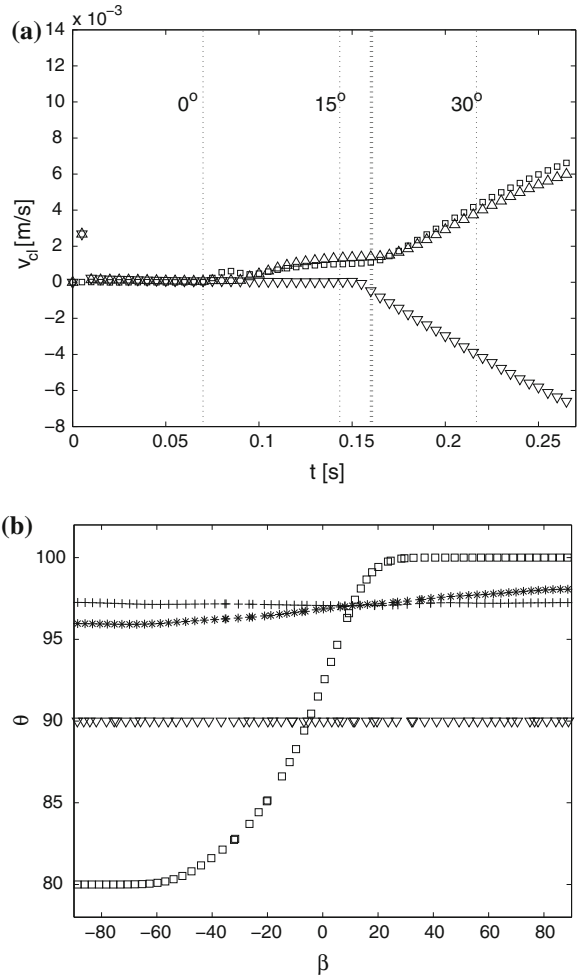

Fig. 6 Eo $= 0.63$ and $\theta_A - \theta_R = 100° - 80°$. (*Top*) Contact line velocities at the *front* ($\triangle$), at the rear ($\triangledown$) and at the centre of mass ($\square$). The corresponding inclination of the surface is shown on the *top* of the graph. The angle at the onset of motion $\alpha_c = 18°$ is shown using a *larger dash line*. (*Bottom*) Distribution of the contact angle along the contact line for different inclinations of the surface. $\triangledown$: $\alpha = 0°$; $+$: $\alpha = 9°$; $\square$: $\alpha = 19°$ (close to the starting point). Contact angle θ along the contact line orientation β

The drop shapes are depicted in Figs. 9, 10 for fluids 47V100 and 47V10, respectively. For both fluids the angles $\alpha = 15°$, $\alpha = 50°$, and $\alpha = 90°$ are shown. In accordance with the experiments of Le Grand et al. (2005), different shapes are observed. When increasing the drop velocity (by increasing α and decreasing the viscosity), the shape varies significantly and so we observe rounded, corner, cusp, and pearling drops. For all cases considered, the front contact line remains circu-

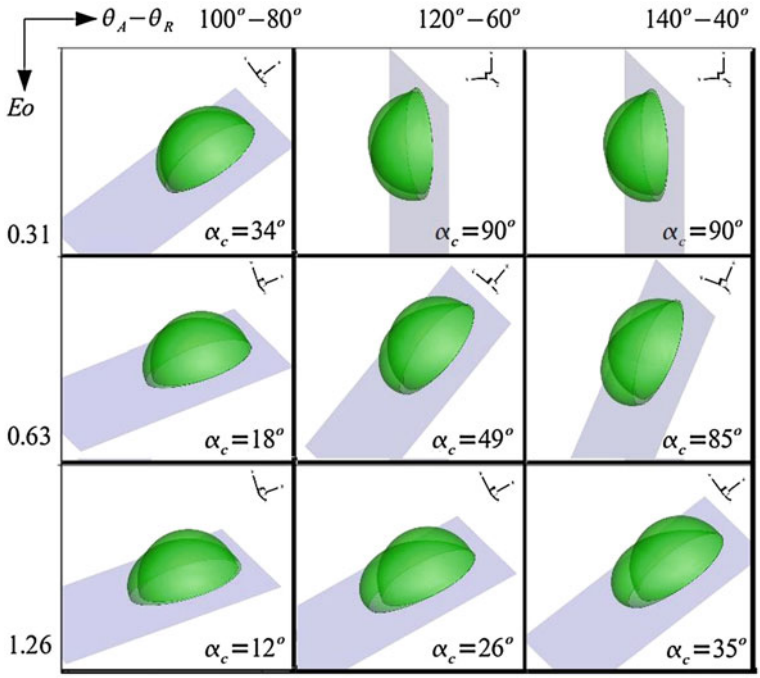

Fig. 7 Drop shapes at the onset of motion compared with the shape at the beginning of the inclination, for different Eötvös numbers and hysteresis ranges. For $\theta_A = 100°$: $\theta_R = 80°$ and Mo = 0.000421; for $\theta_A = 120°$: $\theta_R = 60°$ and Mo = 0.00321; and for $\theta_A = 140°$: $\theta_R = 40°$ and Mo = 0.02568

lar, the difference being mainly noticed at the rear contact line. For the smallest velocities ($\alpha = 15°$ and $\alpha = 50°$ for 47V100 and $\alpha = 15°$ for 47V10), the shape of both the advancing and the receding contact lines is circular. For intermediate velocities, the rear contact line is progressively deformed to form a corner ($\alpha = 50°$ for 47V10) and then a cusp ($\alpha = 90°$ for 47V100). For the largest velocity ($\alpha = 90°$ for 47V10), the pearling regime is observed. The pearling regime is characterized by the emission of droplets from the tip of the cusp. As was reported by Le Grand et al. (2005) (see their Fig. 6), the size of the first droplet is larger than the second one. The transition between the cusp regime and the pearling regime is observed between $\alpha = 60°$ and $\alpha = 70°$ for fluid 47V10. The corresponding capillary number is close to $\mathrm{Ca} = \mu U_T/\sigma \sim 0.01$, in agreement with the experiments of Le Grand et al. (2005).

The time evolution of the drop velocity U for some particular inclinations is shown in Fig. 11 for fluids 47V100 (left) and 47V10 (right), respectively. For both fluids, U increases at the beginning of the simulation, reaches a maximum around $t \sim 0.01$ s, and then decreases and stabilizes to a constant value corresponding to the drop terminal velocity U_T. As expected, the terminal velocity is found to

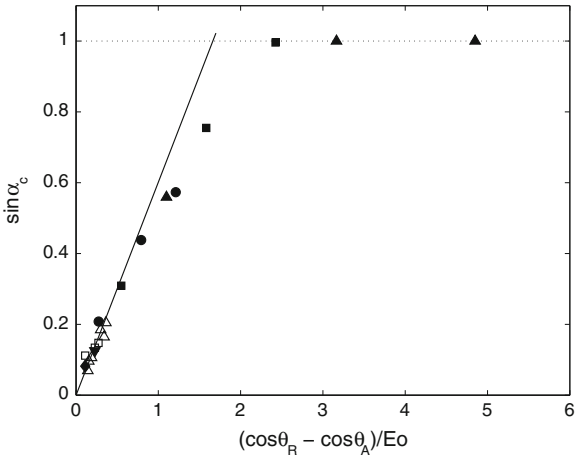

Fig. 8 Variation of the angle $\sin\alpha_c$ with $(\cos\theta_R - \cos\theta_A)\,\mathrm{Eo}^{-1}$. Experiments: □ Le Grand et al. (2005), △ Podgorski (2000). Numerical simulations: ▲ Eo = 0.32 (FL1), ■ Eo = 0.63 (FL2), • Eo = 1.26 (FL3), ▼ Eo = 0.57 (47V100), ▼ Eo = 0.57 (47V100), ♦ Eo = 0.58 (47V10),— $\sin\alpha_c \approx 0.6(\cos\theta_R - \cos\theta_A)\,\mathrm{Eo}^{-1}$ derived from relation (20) (Dussan 1985) with $\kappa_c = 2^{4/3}\,a$, · · · · drop sticked on a vertical surface

increase with α. Figure 11 (right) shows that the velocity is not perfectly stabilized for the less viscous fluid 47V10 with the largest angles $\alpha = 70°$ and $\alpha = 90°$. This is due to the pearling observed at the rear of the drop. The inspection of the first part of the evolution reveals that the evolution of the centre of mass follows $V \sim g\,\sin(\alpha)\,t$. It corresponds to the volume acceleration inside the drop due to gravity. The drop deforms and the front and rear contact angles evolve from the initial value $\theta_S = 50°$ to the advancing and receding contact angle θ_A and θ_R, respectively. Thus, during this first phase of the evolution, the advanced and receding contact lines remain immobile and the drop sticks on the surface. Once the drop deformation has induced values for both the front and rear contact angle outside the hysteresis range (see previous section), the drop starts to slide until it reaches the terminal velocity U_T. The drop Reynolds number $\mathrm{Re} = \rho U_T a/\mu$, based on the terminal velocity, as obtained for $\alpha = 90°$, is $\mathrm{Re} = 0.035$ and 2.8 for fluids 47V100 and 47V10, respectively, evidencing a viscous dominated situation. As a consequence, the contact line Reynolds number $\mathrm{Re}_{cl} = \rho U_{cl} L/\mu \sim \rho U_T \Delta/\mu$ is much smaller than unity, in agreement with the range of validity of the Cox's hydrodynamic model for the apparent contact angle [relation (9)].

The terminal velocity U_T results from the following force balance:

$$\rho g V \sin\alpha - \kappa\sigma(\cos\theta_R - \cos\theta_A) + F_D = 0, \tag{21}$$

where F_D is the drag force experienced by the drop. In F_D we can identify two different viscous contributions. The first corresponds to the bulk contribution F_D^{bulk},

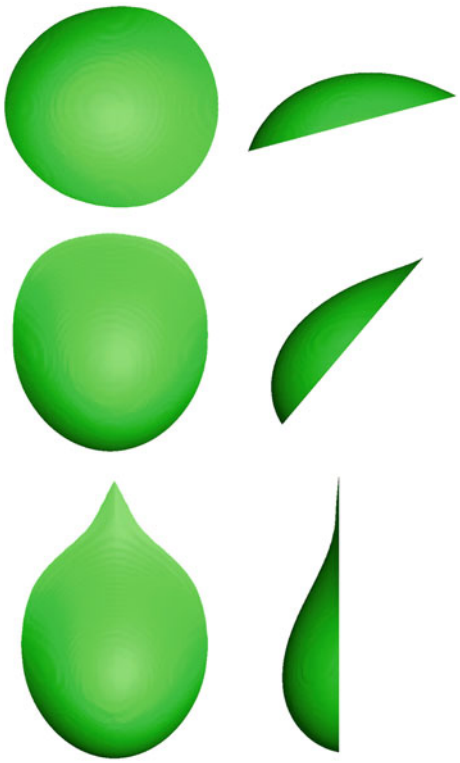

Fig. 9 Drop shape when the terminal velocity is achieved for fluid 47V100 at different inclinations. First column: view normal to the wall. Second column: side view. *Top* $\alpha = 15°$, middle $\alpha = 50°$, *bottom* $\alpha = 90°$

resulting from the viscous effects at the macro scale L. This effect comes from the internal motion and the viscous stress in the air. The second is the contact line contribution F_D^{cl}, which results from the viscous dissipation at the contact line. The drop terminal velocity can be simply derived from the force balance (21) when considering the two following assumptions. The dissipation at the contact line is negligible compared to the bulk dissipation, i.e. $F_{bulk} \gg F_{cl}$ and the drop motion is controlled by viscous effects, i.e. Re$<$ 1. Under such conditions, the drag force experienced by the drop can be written as:

$$F_D \approx F_{vi} \approx -C\mu\pi a U_T, \tag{22}$$

where C is a coefficient depending a priori on the drop shape. Note that for a spherical drop of radius a settling in air, the Stokes drag gives $C = 6$. Assuming that the drop shape during the sliding is similar to its shape at the onset of motion (i.e. $\kappa \approx \kappa_C$), we can write

$$\kappa\sigma(\cos\theta_R - \cos\theta_A) \approx \rho g V \sin\alpha_C$$

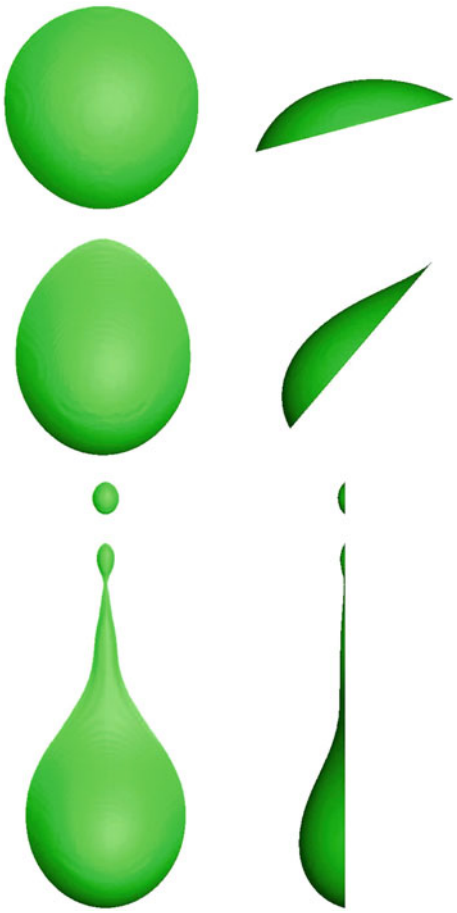

Fig. 10 Drop shape when the terminal velocity is achieved for fluid 47V10 at different inclinations. *First column* View normal to the wall. *Second column* Side view. *Top* $\alpha = 15°$, middle $\alpha = 50°$, *bottom* $\alpha = 90°$

so that the force balance gives the following relation between the capillary and the Eötvös number:

$$\mathrm{Ca} \approx \frac{4}{3C}\mathrm{Eo}(\sin\alpha - \sin\alpha_C). \tag{23}$$

The capillary number is plotted as a function of the Eötvös number in Fig. 12. For both fluids, the linear dependence shows that relation (23) makes possible the description of the sliding velocity. The experimental results of Le Grand et al. (2005) are also depicted for comparison. The figure confirms the good agreement with the predicted value of α_c corresponding to the onset of motion. Figure 12 shows very good agreement with the experiments for the more viscous fluid, 47V100 (left), while a significant deviation is found for fluid 47V10 (right). For fluid 47V100, the evolution is split up into two linear regimes. The first regime agrees with the experiments of Le Grand et al. (2005). Relation (23) fits both the simulation and

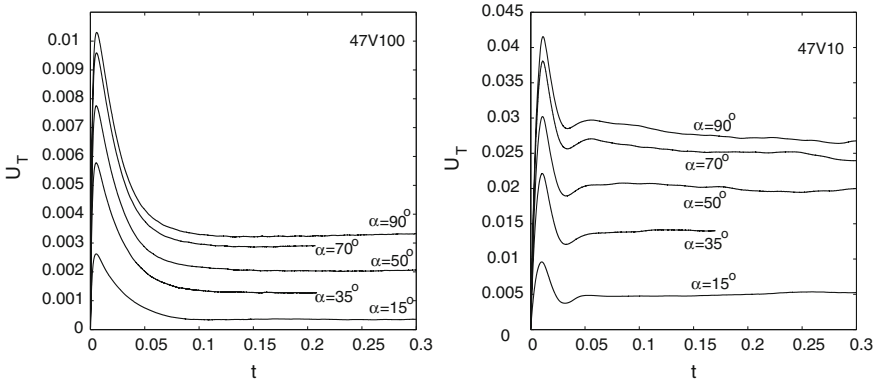

Fig. 11 The time evolution of the drop velocity V for different values of α. From *bottom to top* $\alpha = 15, 35, 50, 70$ and $90°$. (*left*) fluid V100, (*right*) fluid V10

the experiments with $C \sim 83$. On the other hand, the second regime corresponds to $C \sim 50$. This lower value is due to the change of the drop shape. The receding contact line shape generates a lower resistance in the force balance. These values of C show that the drag force experienced by a viscous drop sliding on an inclined wall is one order of magnitude bigger than the one experienced by a settling drop ($C = 6$). For fluid 47V10, relation (23) is also seen to fit the numerical simulation for $C \sim 83$, while the experiments are better described using $C \sim 131$. Our numerical results for fluids 47V100 and 47V10 follow a similar evolution ($C \sim 80 - 83$), while a significant difference is observed with the experiments made with the two fluids. One possible explanation of this discrepancy could be the contact line contribution

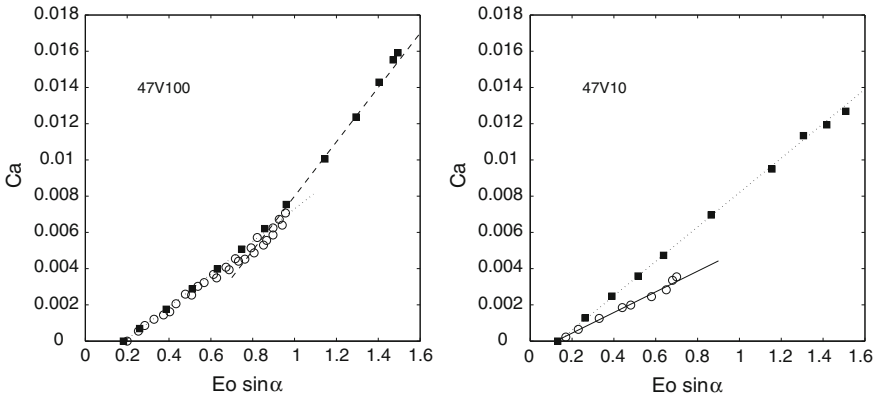

Fig. 12 Evolution of the drop capillary number as a function of the Eötvös number Eo_α. (○) experiments of Le Grand et al. (2005), ■ Numerical simulations. (*left*) fluid 47V100: · · · · $\mathrm{Ca} = 0.009\,\mathrm{Eo}\,\sin\alpha$, - - - $\mathrm{Ca} = 0.015\,\mathrm{Eo}\,\sin\alpha$. (*right*) fluid 47V10: · · · · $\mathrm{Ca} = 0.0095\,\mathrm{Eo}\,\sin\alpha$, —$\mathrm{Ca} = 0.0057\,\mathrm{Eo}\,\sin\alpha$

F_D^{cl} to the drag force. In our simulations, only the large scale dissipation is considered since we do not solve the hydrodynamics at the contact line. While Eq. (9) relates the value of the apparent contact angle to the velocity of the contact line, no sub-grid dissipation was introduced in our models. For the more viscous fluid, the agreement is very satisfactory, suggesting that the main dissipation occurs in the bulk, since F_D^{cl} is small compared to F_{bulk}. For the less viscous fluid, the contribution of F_D^{cl} is more important and could be of the same order of F_{bulk}, resulting in an underestimated drag force in our simulations since the models do not take into account the contribution of F_D^{cl}.

We finally consider the effect of the contact angle hysteresis on the drop sliding velocity. The simulations were performed for fluid 47V100 since the agreement with the experiments was very good. A surface inclination of $\alpha = 50°$ and contact angle hysteresis of (θ_A, θ_R)=(50.5°, 45.5°), (58°, 38°), (63°, 33°), and (68°, 28°) were considered. As expected, the simulations indicate that the sliding velocity decreases when increasing the hysteresis range. Figure 13 depicts the drop capillary number as a function of $\cos\theta_R - \cos\theta_A$. This plot shows that the decrease is linear and reveals that $(\cos\theta_R - \cos\theta_A)$ is again the pertinent parameter for taking into account the hysteresis.

6 Conclusions

We have reported numerical simulations of drops on a inclined solid surface. Both the onset of motion and the sliding regime have been considered. The simulations have compared satisfactorily with the experiments of Le Grand et al. (2005). In addition,

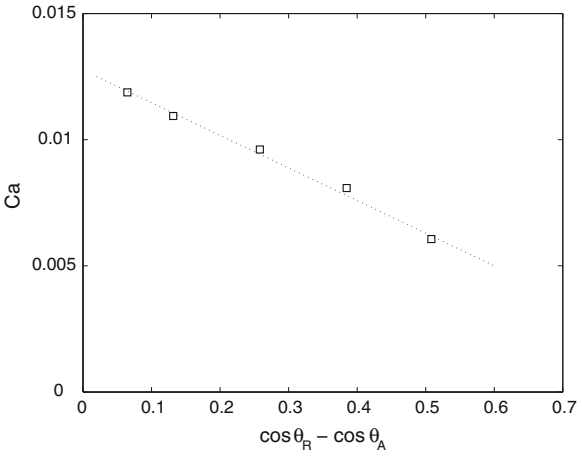

Fig. 13 Effect of the hysteresis on the drop velocity for fluid 47V100 and $\alpha = 50°$. Ca is plotted as a function of $\cos\theta_R - \cos\theta_A$. □ simulations, · · · · $y = 0.0128 - 0.013x$

we have extended the analysis of the effects of the contact angle hysteresis to values of the hysteresis range beyond those usually considered in current experiments. The critical angle of inclination, corresponding to the onset of motion, depends on the Eötvös number, the hysteresis, and the shape of the contact line. When the drop starts to slide, an almost rounded shape is observed in all cases, which contrasts with the very different shapes observed when the drop is sliding. All the experimental and numerical results are found to collapse on the same evolution as shown when $\sin \alpha_c$ is plotted as a function of $(\cos \theta_R - \cos \theta_A)\,\mathrm{Eo}^{-1}$. Regarding the sliding regime, the characteristic shapes observed in the experiments have been recovered by the simulations. Rounded, corner, cusp, and pearling drops have all been observed. The sliding velocity has been found to be in very good agreement with the experiments for the more viscous fluid, while a significant discrepancy has been seen for the less viscous fluid. One possible explanation for this discrepancy are the effects of dissipation at the contact line, which were not included in the present models. A proper inclusion of the effects of dissipation at the contact line is therefore needed to validate this hypothesis. Our study has also stressed the effect of the hysteresis on the sliding velocity. When increasing the hysteresis range, the sliding velocity is found to decrease as $\cos \theta_R - \cos \theta_A$, which appears to be the pertinent parameter for the description of the effects of hysteresis in the sliding motion. Future work will focus on considering the effects of the hysteresis on the different sliding regimes and, in particular, on the pearling regime.

References

Afkhami S, Zaleski S, Bussmann M (2009) A mesh-dependent model for applying dynamic contact angles to VOF simulations. J Comput Phys 228:5370–5389

Bikerman JJ (1950) Sliding of drops from surfaces of different roughnesses. J Colloid Interface Sci 5:349–359

Blake TD (2006) The physics of moving wetting lines. J Colloid Interface Sci 299:1–13

Bonn D, Eggers J, Indekeu J, Meunier J, Rolley E (2009) Wetting and spreading. Rev Mod Phys 81:739–805

Bonometti T, Magnaudet J (2007) An interface capturing method for incompressible two-phase flows. Validation and application to bubble dynamics. Int J Multiph Flow 33:109–133

Brackbill J, Kothe DB, Zemach C (1992) A continuum method for modeling surface tension. J Comput Phys 100:335–354

Cox RG (1986) The dynamics of the spreading of liquids on solid surfaces. Part 1: Viscous flow. J Fluid Mech 168:169–194

Dimitrakopoulos P, Higdon JJL (1999) On the gravitational displacement of three dimensional fluid droplets from inclined solid surfaces. J Fluid Mech 295:181–209

Dupont JB, Legendre D (2010) Numerical simulations of static and sliding drop with contact angle hysteresis. J Comput Phys 229:2453–2478

Dussan EB (1976) The moving contact line: the slip boundary condition. J Fluid Mech 77:665–684

Dussan EB (1985) On the ability of drops or bubbles to stick to non-horizontal surfaces of solids. Part 2. Small drops and bubbles having contact angle of arbitrary size. J Fluid Mech 151:1–20

Dussan EBV, Ramé E, Garoff S (1991) On identifying the appropriate boundary conditions at moving contact lines: an experimental investigation. J Fluid Mech 230:97–116

Extrand CW (1995) Liquid drops on an inclined plane: the relation between contact angles, drop shape, and retentive force. J Colloid Interface Sci 170:515–521
Fang C, Hidrovo C, Wang F, Eaton J, Goodson K (2008) 3-D numerical simulation of contact angle hysteresis for microscale two phase flow. Int. J. Multiph. Flow 34:690–705
Furmidge CGL (1962) I. The sliding of liquid drops on solid surfaces and a theory for spray retention. J Colloid Sci 17:309–324
Huh C, Scriven LE (1971) Hydrodynamic model of the steady movement of a solid/liquid/fluid contact line. J Colloid Interface Sci 35:85–101
Lafaurie B, Nardone C, Scardovelli R, Zaleski S, Zanetti G (1994) Modelling merging and fragmentation in multiphase flows with surfer. J Comput Phys 113:134–147
Lauga E, Brenner MP, Stone HA (2007) Microfluidics: the no-slip boundary condition. In: Tropea C et al (ed) Handbook of experimental fluid dynamics, Chap. 19. Springer, NY, pp 1219–1240
Le Grand N, Daerr A, Limat L (2005) Shape and motion of drops sliding down an inclined plate. J Fluid Mech 541:293–315
Legendre D, Maglio M (2013) Numerical simulation of spreading drops. Colloids and Surf A 432:29–37
Maglio M (2012) Numerical simulation of spreading, sliding and coalescing drops on surfaces. PhD thesis, Institut National Polytechnique de Toulouse, France
Marsh JA, Garoff S, Dussan EB (1983) Dynamic contact angles and hydrodynamics near a moving contact line. Phys Rev Lett 70:2778–2782
Milinazzo F, Shinbrot M (1988) A numerical study of a drop on a vertical wall. J Colloid Interface Sci 121:254–264
Ngan CG, Dussan EB (1989) On the dynamics of liquid spreading on solid surfaces. J Fluid Mech 209:191–226
Podgorski MT (2000) Ruissellement en conditions de mouillage partiel. PhD thesis, Université Paris 6, France
Popinet S, Zaleski S (1999) A front-tracking algorithm for accurate representation of surface tension. Int J Numer Meth Fluids 30:775–793
Renardy M, Renardy Y, Li J (2001) Numerical simulation of moving contact line problems using a volume-of-Fluid method. J Comput Phys 94:243–263
Rio E (2005) Gouttes, Flaques et Arches sèches: Des lignes de contact en présence d'un ècoulement. PhD thesis, Université Paris 6, France
Rotemberg Y, Boruvka L, Neumann W (1984) The shape of nonaxisymmetric drops on inclined planar surfaces. J Colloid Interface Sci 102:424–434
Scardovelli R, Zaleski S (1999) Direct numerical simulation of free surface and interfacial flow. Annu Rev Fluid Mech 31:567–603
Sethian J (1999) Level set methods and fast marching methods. Cambridge University Press, Cambridge
Shen C, Ruth DW (1998) Experimental and numerical investigations of the interface profile close to a moving contact line. Phys Fluids 10:789–799
Spelt PDM (2005) A level-set approach for simulations of flows with multiple moving contact lines with hysteresis. J Comput Phys 207:389–404
Sussman M, Fatemi E, Smereka P, Osher S (1998) A level set approach for computing solutions in incompressible two-phase flows. J Comput Phys 27:663–680
Voinov OV (1976) Hydrodynamics of wetting. Fluid Dyn 11:714–721
Winkels KG, Weijs JH, Eddi A, Snoeijer JH (2012) Initial spreading of low-viscosity drops on partially wetting surfaces. Phys Rev E 85:055301(R)
Yokoi K, Vadillo D, Hinch J, Hutchings I (2009) Numerical studies of the influence of the dynamic contact angle on a droplet impacting on a dry surface. Phys Fluids 21:072102
Zalesak S (1979) Fully multidimensional flux-corrected transport algorithms for fluids. J Comput Phys 31:335–362